UCRL- 93267
PREPRINT

MODEL ATMOSPHERES FOR X-RAY BURSTING NEUTRON STARS

Richard A. London and W. Michael Howard
University of California
Lawrence Livermore National Laboratory
Livermore, CA 94550

Ronald E. Taam
Dept. of Physics and Astronomy
Northwestern University
Evanston, IL 60201

This work was prepared for submittal to
The Astrophysical Journal

August 1985

Model Atmospheres for X-Ray Bursting Neutron Stars*

Richard A. London,[1] Ronald E. Taam,[1,2]
and W. Michael Howard[1]

Received:

*Work performed under the auspices of the U. S. Department of Energy by the Lawrence Livermore National Laboratory under contract No. W-7405-ENG-48.

[1]Univ. of Calif., Lawrence Livermore National Laboratory, Livermore, CA 94550

[2]Dept. of Physics and Astronomy, Northwestern University, Evanston, IL 60201

ABSTRACT

We present the results of seventeen model atmospheres for neutron stars ranging in effective temperature from 0.25 to 3 keV, in gravity from 10^{14} to 10^{15} cm s^{-2}, and in helium and iron abundances. For those models with solar helium abundance, the iron abundances [Fe/H] ranged from 0 to 1 relative to solar. For each model the surface fluxes are tabulated as a function of energy.

It is found that the spectrum significantly differs from a blackbody radiating at the effective temperature. The differences are associated with the effects of surface cooling and backwarming due to the highly non-gray nature of the absorption coefficient mainly important at low effective temperatures, and the depressed emissivity of the source function caused by electron scattering which becomes more important for high effective temperatures. For x-ray burst sources radiating near the Eddington limit, the surface fluxes may be overestimated by as much as a factor of 5 if pure blackbody emission is assumed in interpreting the spectral data.

Bound-free transitions from Fe^{+24} and Fe^{+25} in have been included in the calculations. It is found that Non-LTE effects overionize the iron relative to the LTE ionization balance. As a result, the K-shell absorption edges at about 9 keV are found to be weak for solar metal abundances and for effective temperatures near 1 keV.

I. INTRODUCTION

Since the discovery of the x-ray burst phenomenon by Grindlay et al. (1976), x-ray bursts have become the subject of intense observational and theoretical study. The characteristics of the x-ray bursts include rise time scales between 0.1 and 5 s, durations of 3 to 100 s, and luminosities of about 10^{38} ergs s^{-1} in which a total energy of 10^{39} ergs is emitted. The majority of the available low resolution data can be fit by blackbody spectra which harden during the rise to several keV and soften during decay. For a detailed review of the observational data see Lewin and Joss (1983).

The nature of the source and the mechanism responsible for the x-ray burst are now well established. Based upon the inferred size of the emitting region (~ 10 km, Swank et al. 1977; Hoffman et al. 1977) a neutron star origin is favored. Direct observational evidence on the astrophysical site of the phenomena is provided by the detection of periodic x-ray eclipses every 7.1 hr in MXB 1659-29 (Cominsky and Wood 1984) and nearly periodic absorption dips every 50 min in MXB 1916-053 (Walter et al 1982; White and Swank 1982). Because of the success of the thermonuclear flash model (see reviews by Joss and Rappaport 1984; and Taam 1984, 1985) in reproducing the energetics, temporal structure, and spectral behavior of an average x-ray burst source, it is generally accepted that the x-ray outbursts are caused by thermonuclear shell flashes occurring in the accreted layers of a neutron star.

Although the thermonuclear model is capable of explaining the gross characteristics of x-ray bursts, upon closer scrutiny, there remain several outstanding theoretical problems. Specifically, there is observational evidence based upon distance determinations and spectral data which suggests that the Eddington luminosity for a 1.4 $M_\odot$ neutron star is exceeded in some sources. We do not discuss the super Eddington luminosity evidence based on source distances. Of paramount concern, here, is the problem of the high spectral temperatures characterizing the radiation emitted at and near the burst maximum. Typically, the peak spectral temperatures are observed to be ~ 2.5 - 3 keV in comparison to the maximum Eddington temperature (corrected for general relativistic effects) of 2 keV for current theoretical models (Marshall 1982). Therefore, super Eddington fluxes are indicated if neutron stars are perfect blackbody emitters and if we accept structure models based on current theories for the hadron interaction at high densities and general relativity.

However, in a previous paper (London, Taam, and Howard 1984, hereafter referred to as Paper I), we presented the theory for the continuum spectrum and demonstrated that the neutron star does not radiate as a perfect blackbody during any part of the x-ray burst (see also, Czerny and Sztajno 1983; van Paradijs 1982). That is, the calculated spectra are always shifted to higher energies from that of a blackbody of the same effective temperature. In the low temperature regime (where the effective temperature is much less than the Eddington temperature) the deviation of the spectral temperature from the effective temperature is dependent upon the surface cooling and backwarming effect associated with the strong frequency dependence of the opacity. On the other hand, very near the Eddington temperature the thermalization occurs at optical depths greater than unity where the temperature is higher than the effective temperature. In the latter case the photons are thermalized at a scattering optical depth of order 5 yielding spectral hardening factors (T_{spec}/T_{eff}) ranging up to about 1.5 - 1.6. Although Comptonization is important in determining the spectrum in these cases, its tendency to reduce the high energy part of the spectrum is more than compensated by the fact that the emissivity is depressed (by factors of up to 5 in some cases).

In this paper we present the surface fluxes of individual neutron star model atmospheres in tabular form in order to facilitate comparison of theory to observational data (see Appendix). In section II the basic assumptions, input physics, and equations are given. The numerical results are presented in section III and discussed in section IV. Finally, we summarize our results and make some concluding remarks in the last section.

II. FORMULATION OF THE PROBLEM

We consider the classical model atmosphere problem as applied to the x-ray bursting neutron stars. Here, the atmosphere is characterized by a mass column density of about 10^2 - 10^3 g cm^{-2} which ensures that the matter and radiation are well thermalized at the base. We assume that the atmosphere is in a steady state and in radiative equilibrium. The former assumption is well justified since the hydrodynamical and thermal timescales within the atmosphere are much shorter than the timescales over which the observed fluxes vary. Energy transport by means other than radiation (e.g. convection) are unimportant and are neglected. Since radiative fluxes less than the critical Eddington flux will only be considered, the pressure stratification in the atmosphere is determined by the hydrostatic equilibrium condition. In such a case the atmosphere will be geometrically thin compared to the neutron star radius to within one part in 10^4.

Effects associated with chemical composition inhomogenities, magnetic fields, and accretion taking place during the x-ray burst on the structure of the atmosphere are ignored in this work. Based upon the study of Fontaine and Michaud (1979), as applied to neutron stars, the timescales for elemental diffusion through the atmosphere are comparable to the replenishment timescale by accretion for mass transfer rates of about 10^{-11} $M_{\odot}$ yr^{-1}. Since the mass transfer rates in the x-ray burst sources are probably of the order of 10^{-9} $M_{\odot}$ yr^{-1}, the neutron star atmospheres are expected to be chemically homogeneous to a good approximation. We neglect magnetic effects on the opacity and on the hydrostatic structure of the atmosphere in order to study the radiative transfer effects in the lowest, nontrivial, approximation. Based upon the work of Chanmugam (1980) the cyclotron opacity exceeds the free-free opacity in the x-ray regime for field strengths greater than about 10^{11} Gauss. The neglect of the magnetic effects on the pressure balance , however, provides the more stringent upper limit on the surface field strength of the neutron star and is about 10^{8} gauss. Our assumption is justified in part by the fact that there is little observational evidence for large scale magnetic fields. Finally, the effect of accretion on the atmosphere is expected to be minimal since the ram pressure of the accretion flow is at least an order of magnitude less than the photospheric pressure.

To facilitate the construction of the atmospheric models, the time dependent equations of radiation transport and hydrodynamics were solved. From an initial static Rosseland mean radiative equilibrium structure, the solutions were evolved in time until a steady state was achieved. The equations and the numerical method which are used for radiation transport are described in a paper by Axelrod, Dubois, and Rhoades (1984). The time and frequency dependent radiation transport equation is written as

$$\frac{\partial U_\nu}{\partial t} = - \nabla \cdot F_\nu^r + c\sigma_\nu^a (T_e) [r B_\nu(T_e) - U_\nu] + S_\nu + W_\nu \tag{1a}$$

where the factor, r, is unity in LTE and is equal to the emissivity divided by $\sigma_\nu^a B_\nu$ in non-LTE. The radiative flux F_ν^r is given by

$$F_\nu^r = D_\nu^r \ \nabla U_\nu \tag{1b}$$

with D_ν^r, the diffusion coefficient expressed as

$$D_\nu^r = \frac{c}{3(\sigma_\nu{}^a + \sigma_\nu{}^s)} \ . \tag{1c}$$

The electron temperature, T_e, is determined from

$$\rho C_V^e \frac{\partial T_e}{Mt} = - \nabla \cdot F^e - c \int \sigma_\nu^a(T_e)[r B_\nu (T_e) - U_\nu] d\nu - \int S_\nu d\nu + \omega^{ie} (T_e) (T_i - T_e) C_V^i \rho + S^e/\rho \tag{1d}$$

and the ion temperature, T_i, is determined by

$$\rho C_V^i \frac{\partial T_i}{\partial t} = - \nabla \cdot F^i + \omega^{ie} (T_e) (T_e - T_i) C_V^i \rho + S^i/\rho \tag{1e}$$

The following quantities are: U_ν, the radiation energy density at frequency ν; $B_\nu(T)$, the Planck energy density at temperature T at frequency ν; F^e and F^i, the energy flux from electron and ion heat conduction; S_ν, the energy flow rate into frequency ν from Compton scattering with thermal electrons; W_ν, the rate of energy flow into frequency ν from hydrodynamic work on radiation; C_V^e, C_V^i the specific heat at constant volume for the electrons and ions respectively; σ_ν^a, the absorption opacity per unit length at frequency ν, σ_ν^s, the electron scattering opacity; S^e, and S^i, the rates of energy flow to electrons and ions from hydrodynamic work; ω^{ie}, the electron ion coupling, and ρ the matter density. In our model calculations the conductive fluxes are negligibly small compared with the radiative fluxes and the electron and ion temperatures are essentially equal.

The hydrodynamic equation is

$$\rho\frac{dV}{dt} = -\nabla P - g + \frac{1}{c}\int\rho(\sigma_\nu^a + \sigma_\nu^s) \cdot F_\nu^r \, d\nu \tag{2}$$

where V is the velocity, P the gas pressure, and g is the gravitational acceleration at the neutron star surface. Eq. (2) is constrained to satisfy the boundary conditions that the velocity equals zero at the base and that the gas pressure approaches zero at the surface.

The radiation transport equations, Eqs. (1a) and (1b), are formulated numerically in terms of a multi-frequency diffusion approximation. These equations are solved subject to the boundary conditions of constant temperature black body radiation at the bottom of the atmosphere and of no incident radiation at the top. For this specific problem we have found that the use of the simple (Eddington) diffusion operator is more accurate than the flux-limited operator given by Axelrod et al (1984). The sources of opacity include contributions from inelastic (Compton) electron scattering, free-free processes due to ionized H and He, and bound-free K shell transitions from Fe^{+24} and Fe^{+25} with the absorption coefficients of the latter obtained from Bethe and Salpeter (1957). With the exception of iron, the gas is assumed to be fully ionized. Non-LTE effects have been included in calculating the ionization equilibrium assuming a single bound level each for Fe^{+24} and Fe^{+25}. The processes of electron collisional ionization (with rates adopted from Seaton 1964) and photo-ionization and their inverses are included. We consider the equation of state to be one of a perfect ideal gas supplemented by contributions due to radiation.

Comptonization is handled with a temperature dependent redistribution matrix containing the probabilities for photons to scatter from one frequency bin to another. To conserve computer memory and time, only nearest bin couplings are kept in the matrix. This requires the bin spacing to be large compared to the average frequency shift per scattering. The matrix elements ($R_{i,j}$) are determined from cross-sections for spontaneous up and down scattering ($\sigma_{i,j}$):

$$R_{i,j} = (1 + N_j)\ \sigma_{i,j}/\sigma_i^s;\ j = i \pm 1, \tag{3}$$

where N_i, the photon occupation number at frequency ν_i, accounts for stimulated scattering. Two sets of equations are solved to find $\sigma_{i,j}$:

$$(\nu_{i+1} - \nu_i)\ \sigma_{i,i+1} - (\nu_i - \nu_{i-1})\ \sigma_{i,i-1} = \langle\sigma\Delta\nu\rangle_i \tag{4}$$

and

$$W(\nu_i)\ \sigma_{i,i+1} = W(\nu_{i+1})\ \sigma_{i+1,i}. \tag{5}$$

Here $\langle\sigma\Delta\nu\rangle_i$ is the cross section weighted average frequency shift and $W(\nu_i)$ is the Wien distribution. Eq. (4) ensure that the redistribution matrix gives the correct average frequency shifts while Eq. (5) guarantees that the correct asymptotic distribution is maintained for a pure scattering problem. The Wien distribution is used, rather than the Planck since only spontaneous emission is included in (σ_{ij}). Eq. (3) includes the stimulated scattering and thus guarantees that the Planck distribution is maintained in the steady state, optically thick limit of the transfer equation. We take $\langle\sigma\Delta\nu\rangle_i$ from an analytic fit to a table of values, each of which has been determined by numerical integration over photon angle and the relativistic Maxwellian electron distribution. Since $\langle\sigma\Delta\nu\rangle_i$ and $W(\nu_i)$ are temperature dependent, (σ_{ij}) are recalculated from Eqs. (4) and (5) as the temperature in each zone changes. Further details of the numerical method are given by Axelrod, Dubois, and Rhoades (1984).

Owing to the use of only nearest neighbor bin couplings, the validity of this technique is limited to temperatures and photon frequencies much less than the electron rest mass; the resolution of the resultant spectra is limited to be larger than the frequency shift per scattering. In this respect the method is similar to the Fokker-Planck formulation (cf. Ross 1979).

Our models typically use between 30 and 40 depth zones logarithmically spaced in column density and 50 logarithically spaced radiation bins. Each time step involves an explicit time advance of the momentum equations followed by an implicit advance of the coupled radiation and internal energy equations. We have found it useful to artificially damp the velocities in the relaxation process. Calculations generally relax in about 10^{-6} to 10^{-4} s of simulated time in 10^2 to 10^3 time steps, taking several minutes of CPU time on a CRAY-1. To verify the accuracy of the code, comparisons were made to analytical spectra for gray models with elastic scattering (Madej 1974), the spectra published by Van Paradijs (1982), and the spectra of Comptonized emission from isothermal spheres, published by Chapline and Stevens (1973). In all three comparisons the emergent spectra agreed to better than 25% at frequencies of interest.

III. NUMERICAL RESULTS

Seventeen model atmospheres were calculated, each characterized by the flux expressed in terms of the effective temperature, the gravity, and the set of elemental abundances. The model parameters are summarized in Table 1. For each model the surface fluxes are listed as a function of frequency in the Appendix. To facilitate the presentation of the numerical results we divide into separate subsections the following discussion of the variation of the spectral temperature as a function of effective temperature, chemical composition, and surface gravity of the neutron star. In addition, we discuss the effect of Comptonization compared to purely elastic scattering.

a) Variation in Effective Temperature

Consider atmospheres characterized by a metal abundance of 10^{-5} times solar (essentially <u>no</u> iron) and gravity of 10^{15} cm s^{-2}. At low effective temperatures (e.g. $T_{eff} < 1.5$ keV) the spectral hardening factor decreases with increasing effective temperature (see Table 1). This trend reflects the dominance of the free-free opacity at these temperatures. The opacity is highly non-gray as it is approximately proportional to ν^{-3}. Since the opacity is high at low frequency ($h\nu < 1$ keV), the flux is redistributed to higher frequencies where it experiences less absorption. In addition, the high emissivities at low frequencies and temperatures lead to surface cooling. These combined effects are illustrated in Figures 1 and 2, for the emergent energy distribution and temperature profiles for the 0.5 keV model. It is seen that the energy distribution is shifted to higher frequencies than a Planck function evaluated at the corresponding effective temperature. The calculated curve can be fit by a Planck function (normalized to preserve the flux), but at a spectral temperature 1.69 times the effective temperature. The fit is approximate, however, since the calculated spectrum is characterized by a broader peak and by an excess flux at lower frequencies. This energy distribution reflects the combination of the normal atmospheric temperature gradient with the frequency dependence of the opacity. The high energy part of the spectrum is formed deep in the atmosphere where the temperature is higher. Note that the gas temperature is only 0.42 times the radiation temperature at the surface, reflecting the dominance of cooling by free-free emission. The radiation temperature approaches the electron temperature to within 2% at a column mass density of about 5 g cm^{-2}.

The spectrum for a hotter model (T_{eff} = 1.5 keV) is shown in Figure 3. Here the spectral hardening factor is 1.43, somewhat less than the preceeding case as scattering diminishes the surface cooling-backwarming effect.

With an increase in effective temperature from 1.5 to 2 keV the relative contribution of electron scattering to the total opacity increases, the opacity becomes less frequency dependent and the spectral hardening factor tends to level off. Upon comparison of models 13 with 14, a further increase in effective temperature to 2.5 keV, however, results in an increase in the spectral hardening factor from 1.40 to 1.45. Here, the radiation transport is dominated by scattering, but the thermalization is due mainly to free-free processes. The net result is that the thermalization occurs at optical depths greater than unity where the temperature is greater than the effective temperature. For example, the temperature structure for model 14 is illustrated in Figure 4 where it is found that thermalization depth occurs at a column mass density of about 15 g cm^{-2} corresponding to an electron scattering optical depth of about 5. Note that the thermalization depth is much deeper in the atmosphere for the higher effective temperature models, reflecting the fact that the absorption opacities are lower at the frequencies where most of the energy is emitted. Comptonization is already of some importance in this model, as indicated by the fact that the electron temperature increases in the outermost atmospheric layers. In contrast to the lower effective temperature models, surface heating is more important than surface cooling, with the matter temperature exceeding the radiation temperature at the surface by a factor of 1.57 in model 14. In this case there is a tendency for the gas to approach the spectral temperature due to Compton energy exchange.

For effective temperatures greater than 2.5 keV the spectral hardening factor increases as the Eddington limit is approached; however, the particular process responsible for the thermalization of the radiation field is different At effective temperatures near the Eddington temperature (e.g. model 15) free-free processes are less important as Compton recoil and doppler processes are far more effective in transferring energy.

b) Variation in Metal and Hydrogen Abundance

Consider an atmosphere of solar metal abundance and gravity of 10^{15} cm s^{-2}. The variation of the spectral hardening factor with metal abundance for a given effective temperature and surface gravity is slight. Its greatest influence is bound to occur at effective temperatures < 2 keV where Fe is not fully ionized. Upon comparison of model 10 with 9 or model 12 with 11 in this temperature regime it is found that the spectral hardening factor decreases by 3% to 4% with the inclusion of a solar iron abundance. The difference stems from the fact that there is more opacity in the high energy part of the spectrum due to the iron resulting in a greater flux emitted shortward of 8.8 keV where the opacity is lower. The energy distribution for model 10 is shown for comparison with model 9 in Fig. 5. It is clear that the high energy part of the spectrum is reduced in the solar case relative to the metal poor case. This results in a greater spectral hardening factor for the low metal case than for the solar metal case. For effective temperatures near the Eddington temperature, the iron is completely ionized and the energy distribution and the structure of the atmospheres become independent of the metal abundance.

In paper I, it was found that the iron absorption feature was strong in the LTE approximation for solar or near solar metal abundances and for effective temperatures ~ 1-1.5 keV. However, upon comparison of the radiative ionization rates with the collisional ionization rates for Fe it is found that Non-LTE effects are important. In the non LTE approximation on the other hand, the degree of iron ionization is increased for a given effective temperature and gravity, leading to weak absorption features. This is a direct result of the fact that the radiation field at frequencies above the K-edges (~9 keV) is much stronger than the local Planck function because of the spectral hardening effect (see Fig. 5). The source function for the bound-free transitions, being radiation dominated, is therefore much larger than the Planck function and the thermalizing effect is greatly reduced from what it would be in LTE.

Model 17 was calculated with all helium at an effective temperature of 2.8 keV and gravity of 10^{15} cm s^{-2} to determine the dependence of the hydrogen composition on the spectrum. From Table 1 it is seen that the spectral hardening factor is reduced by a small amount from 1.52 to 1.39. For this model thermalization is achieved at shallower depths than in the corresponding hydrogen rich model (see section IV).

c) Variation in Gravity

Atmospheric models with $g = 10^{14}$cm s^{-2} were constructed in order to study the sensitivity of the spectral hardening factor to variations in the surface gravity of the neutron star. For high effective temperatures, the spectral hardening factor is larger for smaller gravities since the densities are lower, resulting in larger thermalization depths. In these atmospheres electron scattering plays a greater role in the radiation transport. However, if we normalize the effective temperature to the Eddington temperature it is found that the dependence of the spectral hardening factor is exceedingly weak (see below). For example, the spectral hardening factors are 1.52 and 1.55 for models 15 and 6 characterized by a ratio of effective temperature to Eddington temperature of 0.92 and 0.94 respectively.

d) Effect of Comptonization

Finally we conclude this section by discussing the importance of Comptonization relative to coherent electron scattering. In Fig. 6 we illustrate the spectrum for models (15 and 16) characterized by an effective temperature of 2.9 keV, solar metal abundance, and a surface gravity of 10^{15} cm s^{-2} calculated with and without Comptonization respectively. Upon comparison of these two models it is immediately clear that the spectrum calculated with Comptonization is shifted considerably to lower energies with respect to the model calculated with electron scattering assumed to be elastic. This emphasizes the importance of Comptonization in the radiation transfer process. Although the spectrum is shifted to lower energies relative to the non-Comptonized case, the spectrum still peaks at higher energies relative to a Planck function evaluated at the effective temperature. Note that the Comptonized spectrum is well fit by a Planck function at a spectral temperature of 4.3 keV at high energies (> 3 keV), but the calculated spectrum is in excess of the Planck function at lower energies (< 1 keV).

IV. DISCUSSION

In the following discussion we concentrate upon the physics of the atmospheric structure in order to provide a physical understanding of the spectrum. Much of our understanding can be obtained from an analysis of the atmospheric structure based upon an Eddington gray approximation. In particular, we assume that the temperature, T, can be expressed as a function of a frequency averaged optical depth, τ, as

$$T = T_{eff} \left[\frac{3}{4} (\tau + 2/3)\right]^{1/4} \quad (6)$$

In what follows it will be convenient to divide the discussion into various regions in the effective temperature - surface gravity plane (see paper I) delineated by the curves T_1, T_2, T_3, and T_4 (see fig. 7).

Consider region A ($T < T_1$) where electron scattering is unimportant and where the (free-free) opacity declines sharply with increasing frequency. The surface flux at each frequency is approximately proportional to the Planck function at τ_ν equal to unity (the "Eddington-Barbier relation"). Since the high energy part of the spectrum is formed at greater depths (i.e. corresponding to higher temperatures), the mean intensity at the surface decreases less rapidly with increasing frequency than a Planck function evaluated at the effective temperature. Thus, the strongly frequency dependent absorption is responsible for producing a harder spectrum even for effective temperatures significantly less than the Eddington limit.

This general tendency is further enhanced by the affect of the non-gray aspect of the absorption on the temperature structure. As shown in the previous section, backwarming at the lower frequencies steepens the temperature gradient in the atmosphere to allow more of the flux to be emitted at higher frequencies to satisfy the radiative equilibrium constraint. The spectral hardening is, in part, a consequence of this flux redistribution.

The amount of the shift to higher frequencies is also affected somewhat by the bound-free transitions associated with partially ionized iron atoms. In those cases, the flux in the high energy part of the spectrum ($h\nu \sim 9$ keV) is absorbed and redistributed to lower frequencies. However, the numerical results reveal that the effect of the sharply declining opacity (associated with free-free processes) over most of the spectrum dominates to produce an overall hardening of the spectrum relative to the Planck function at the effective temperature.

In the intermediate region B, scattering begins to play a role in spatial transport, diminishing the surface cooling-backwarming effect of pure free-free opacity. For effective temperatures greater than about 1-1.5 keV ($T_2 < T < T_3$; region C) electron scattering dominates the spatial transport and the opacity becomes grayer, with backwarming playing a lesser role. Free-free still dominates the gas-radiation energy exchange. By solving the frequency dependent transfer equation with Eq. (6) as the temperature distribution, one finds that the emergent flux has approximately the shape of the Planck function at temperature T_{spec} defined at τ_{th}, where

$$\tau_{th} = [(\sigma^a + \sigma^s)/3\sigma^a]^{1/2} \tag{7}$$

is the thermalization depth. Here, κ and σ^a and σ^s are the absorption and Thompson scattering opacities, assumed to be constant and gray. The spectrum is harder than a Planck function at the effective temperature due to the depression of the source function introduced by the scattering. Since the absorption opacity is, in reality, neither constant nor gray, an average value is used. For the purposes of our discussion we use a Kramers form for the free-free opacity evaluated at the temperature and density corresponding to the thermalization depth, and at the frequency of the Planck maximum at that temperature:

$$\sigma^a = 0.123\ \rho T^{-7/2} \mu_e^{-1}, \tag{8}$$

where T is the temperature in keV and μ_e is the mass per electron relative to the proton mass. We note that the numerical coefficient in the above equation depends upon the choice for the frequency and would be modified if, for example, a Rosseland mean average value were chosen. The density is obtained from the equation of hydrostatic equilibrium supplemented by the ideal gas law:

$$\rho = 0.104\ \mu\ g_* \tau\ /(\sigma^s T) \tag{9}$$

where μ is the mass per particle measured in proton masses and g_* is the effective gravity (after subtraction of the radiative acceleration) in units of 10^{14} cm s^{-2}. We have made the assumption that the scattering dominates the opacity. By solving Eqs. (6-8) we find for the spectral hardening factor

$$\frac{T_{spec}}{T_{eff}} = 1.18\ T_{eff}^{3/5}\ g_*^{-2/15} a\ , \tag{10a}$$

where a is a composition dependent factor equal to unity for pure H and 0.8 for pure He. The above relation illustrates that when coherent scattering dominates the opacity the spectral hardening increases with effective temperature and decreases with gravity and hydrogen abundance. The variation of the spectral hardening factor with effective temperature from equation (10a) is found to be slightly steeper than indicated by the numerical results for region 3; however,it reproduces the spectral hardening factor to within 15%. Expressing the effective temperature in terms of the Eddington temperature we find

$$\frac{T_{spec}}{T_{eff}} = 1.76 \left(\frac{T_{eff}}{T_{Edd}}\right)^{3/5} \left(1 - \left(\frac{T_{eff}}{T_{Edd}}\right)^{4} \right)^{-2/15} g_{*}^{1/60} a' , \qquad (10b)$$

where a' is equal to 0.9 (0.8) for pure hydrogen (helium). The spectral hardening factor re-written in this way is less dependent upon composition and is only weakly on gravity (see section IIIc).

To be complete, at higher effective temperatures and lower gravities (i.e., as the Eddington temperature is approached; $T > T_3$, denoted as region D which borders on our most extreme models), Comptonization is dominant in thermalizing the radiation and Eqs. (10a) and (10b) are no longer valid. In this case the thermalization depth can be estimated by considering the spatial transport of a highly Comptonized spectrum. For the Compton y parameter much greater than unity where

$$y = \frac{kT\tau^2}{m_e c^2} \qquad (11)$$

the photons emitted by the free-free process at small frequencies are completely upscattered to a Bose-Einstein distribution (Kompaneets, 1957; Illarionov and Sunyaev 1972). In the asymptotic limit ($y > y_c \sim 10^4$; where

$$y_c = \frac{kT}{m_e c^2} \frac{\sigma^s}{\sigma^a} \frac{1}{3A} \qquad (12)$$

the Bose-Einstein approaches a Planck distribution (see Illarionov and Sunyaev 1975 and Rybicki and Lightman 1981). In Eq. (12) A is the Compton enhancement factor, written as

$$A = \frac{3}{4} \ln^2 \left(\frac{2.35}{\xi_e}\right) \tag{13}$$

where ξ_e is the energy (in units of kT) for which the rates of the Compton processes and the free-free processes are comparable. For $\xi_e \ll 1$ as in the present case, we have

$$\xi_e = 3.8 \times 10^{17} \rho^{1/2} T^{-9/4} . \tag{14}$$

The thermalization depth is obtained by inverting equation (11) with y equal to y_c:

$$\tau_{th} = (\sigma^S/3A\sigma^a)^{1/2} \tag{15}$$

For depths less than that given by equation (15), the matter is forced to be isothermal at the spectral temperature because of the strong Compton heating and cooling. At greater depths the matter and temperature distribution follow that given by the gray temperature distribution [eq. (6)]. By matching the isothermal outer region with the inner, gray temperature region, we find the specific value of the thermalization depth and spectral temperature. Combining Eqs. (6), (8), (9), and (15) in this manner yields an estimate of the spectral hardening factor for region D:

$$\frac{T_{spec}}{T_{eff}} = 1.14\, T_{eff}{}^{3/5}\, g_*{}^{-2/15}\, a/\ln^{4/15} \left(\frac{2.35}{\xi_e}\right) . \tag{16}$$

This expression is valid only in the asymptotic limit and is not directly applicable to our results. If, however, we apply it to our most extreme models we find that the spectral hardening factor as given by equation (16) overestimates the calculated results by about 50%. The analysis shows that the spectral hardening factor should increase right up to the Eddington limit.

V. CONCLUSIONS

Self-consistent neutron star atmospheric models have been constructed which include the effects of Comptonization, free-free and bound-free absorption. It has been demonstrated that for parameters relevant to x-ray bursting neutron stars the atmosphere does not radiate like a blackbody during any phase of an x-ray burst. In particular, during the initial rise and final decline of the burst the temperature structure of the atmosphere is affected by backwarming associated with the high opacity due to free-free processes at low frequencies to an extent that the radiation spectrum is shifted to higher energies than a blackbody of the same effective temperature. On the other hand, near the peak of the burst, the opacity is more gray like as the electron scattering opacity dominates; however, in this case thermalization of the radiation field occurs at such large optical depths ($\tau \sim 5$) that the spectral temperature is higher than the effective temperature. This result is found despite the importance of Comptonization in the thermalization process. Thus, the super Eddington fluxes implied by the spectral data alone are misleading and result from the improper use of the spectral temperature for the effective temperature. For neutron stars characterized by a soft equation of state and radiating near the Eddington effective temperature fluxes obtained in this way could be overestimated by a factor of about 5.

Because the spectral hardening factor varies throughout an x-ray burst, deconvolution of the spectrum is required before definitive statements can be made concerning the variation of the size of the emitting region. We may say that because of the spectral hardening effect, radius determinations, based on the spectral temperature are only lower limits.

We have also found that the shape of the continuum can be affected by the presence of Fe in the atmosphere; however, the features associated with bound-free transitions from partially ionized Fe are not particularly strong in the non-LTE approximation for solar abundances.

Since the spectral hardening factors are found to be weakly dependent upon the surface gravity of the neutron star, the detection of features may be the only probe of the gravitational field of the emitting region in the vicinity of the neutron star. The detection of such features (see for example, Waki et. al 1984) may place constraints on the mass radius relation of the neutron star and on the hadron interaction at densities unattainable in the terrestrial laboratory. The possibility that such features could be detected is of great import and it is our intent to study the line formation problem in a future investigation. With such detailed model atmospheres in hand, it may be possible to directly determine the metal abundance of the accreted fuel. Thus, the analysis of the radiation spectrum emitted from x-ray bursting neutron stars with the stellar atmosphere tool may prove just as valuable in determining stellar parameters as it has been found for normal stars.

ACKNOWLEDGMENTS

We have benefitted by conversions with T. Axelrod and G. Canfield. This work was supported in part by the NSF under grant AST81-09826 A01 and was performed under the auspices of the U. S. Department of Energy under contract W-7405-ENG-48, LLNL. The initial stages of this project were formulated at the Summer Workshop on High Energy Transients, held in Santa Cruz, California, July 1983.

REFERENCES

Axelrod, T. S., Dubois, P. F., and Rhoades, Jr. C. E. 1984, J. Comp. Phys., 54, 205..

Bethe, H. A., and Salpeter, E. E. 1957, in Quantum Mechanics of One and Two Electron Atoms (Berlin: Springer Verlag).

Chanmugam, G. 1980, Ap. J., 241, 1122.

Chapline, G. and Stevens, J. 1973, Ap. J., 184, 1041.

Cominsky, L. R., and Wood, K. S., 1984, Ap. J., 283, 765.

Czerny, M., and Sztajno, M. 1983, Acta Astr., 33, 213.

Fontaine, G., and Michaud, G. 1979, Ap. J., 231, 826.

Grindlay, J. Gursky, H. Schnopper, Parsignault, D. R., Heise, J., Brinkman, A. C., and Schrijver, J. 1976, Ap.J. Letters, 205, L127.

Hoffman, J. A., Lewin, W. H. G., and Doty, J. 1977, Ap. J. Letters, 217, L23.

Illarionov, A. F., and Sunyaev, R. A. 1972, Sov. Ast., 16, 45.

Illarionov, A. F., and Sunyaev, R. A. 1975, Sov. Ast., 18, 413.

Joss, P. C., and Rappaport, S. A. 1984, Ann. Rev. Ast. Ap., 22, 537.

Kompaneets, A.S. 1957, Soviet Physics-JEPP., 4, 730.

Lewin, W. H. G., and Joss, P. C. 1983, in Accretion Driven Stellar X-Ray Sources, eds. W. H. G. Lewin and E. P. J. van den Heuvel (Cambridge,England: Cambridge University Press), p. 41.

London, R. A., Taam, R. E. and Howard, W. M. 1984, Ap J. Letters, 287, L27.

Madej, J. 1974, Acta Astr., 24, 327.

Marshall, H. L. 1982, Ap. J., 260, 815.

Ross, R. R. 1979, Ap. J., 233, 334.

Rybicki, G. B. and Lightman, A. P., 1979, Radiative Processes in Astrophysics, (New York: Wiley).

Seaton, M. J. 1964, Planet. Space Sci. 12, 55.

Swank, J. H., Becker, R. H., Boldt, E. A., Holt, S. S., Pravdo, S. H., and Serlemitsos, P. J. 1977, Ap. J. Letters, 212, L73.(1984).

Taam, R. E. 1984, in High Energy Transients in Astrophysics, AIP Conf. Proc. No. 115, ed. S. E. Woosley (New York: AIP Press), p. 263.

Taam, R. E. 1985, Ann. Rev. Nuc. Part. Sci., 35, l.

Van Paradijs, J. 1982, Ast. Ap., 107, 51.

Walter, F. M., Bowyer, S., Mason, K. O., Clark, J. T., Henry, P., Halpern,J., and Grindlay, J. E. 1982, Ap. J. Letters, 253, L67.

White, N. E., and Swank, J. H. 1982, Ap. J. Letters, 253, L61.

Waki, I., et. al., 1984. Publ. Astr. Society of Japan, 36, 819.

FIGURE CAPTIONS

Figure 1. The emergent flux as a function of energy for an atmosphere characterized by an effective temperature of 0.5 keV, surface gravity of 10^{15} cm s^{-2}, and an Fe abundance 10^{-5} times solar (model 8). The solid histogram is the calculated spectrum. The dot-dash curve corresponds to the Planck function evaluated at the effective temperature and the solid curve is the Planck function which best fits the calculated spectrum.

Figure 2. The temperature distribution as a function of column mass density for model 8. The solid curve denotes the matter temperature whereas the dot dashed curve denotes the radiation temperature.

Figure 3. Same as in Fig. 1 for model 11, characterized by an effective temperature of 1.5 keV.

Figure 4. Same as in Fig. 2 for an atmosphere characterized by an effective temperature of 2.5 keV, surface gravity of 10^{15} cm s^{-2}, and 10^{-5} metal abundance (model 14).

Figure 5. The energy distribution for atmospheres characterized by an effective temperature of 1 keV and a gravity of 10^{15} cm s^{-2}. The solid histogram is for solar metal abundance (model 10) while the dashed histogram is for 10^{-5} solar metal abundance (model 9).

Figure 6. The emergent flux from atmospheres characterized by an effective temperature of 2.9 keV, surface gravity of 10^{15} cm s^{-2}, and a solar metal abundance for models with (solid histogram curve, model 15) and without Comptonization (dotted histogram, model 16).

Figure 7. The separation of the surface gravity-effective temperature plane according to the processes responsible for determining the spectrum. Here, $T_1 = 0.3\alpha g_*^{2/9}$ where the scattering opacity equals the Rosseland mean opacity at the scattering photosphere; $T_2=0.9\alpha g_*^{2/9}$ denotes the locus for which the scattering opacity equals the Planck mean opacity at the photosphere; $T_3 = 2.1\beta g_*^{3/16}$ defines the locus for which the energy exchange rates by free-free processes are comparable to the Compton processes at the thermalization depth, and T_4 is the Eddington effective temperature-the maximum value for which static atmospheres exist. The factors α and β are composition dependent and take on the values of unity for pure hydrogen and 1.5 and 1.2 respectively for pure helium. The curves are shown for a pure hydrogen composition.

APPENDIX

We present tables of the surface fluxes for sixteen model atmospheres. Effective temperatures are given in keV, gravities in cm s^{-2} and abundances relative to solar (0.1 for He and 3.4 x 10^{-5} for Fe relative to H by number). Frequencies are in keV and fluxes are in erg cm^{-2} s^{-1} keV^{-1}. The fluxes for the low and high T_{eff} models are in Table 2 while those for mid-T_{eff} are in Table 3.

TABLE 1. MODEL PARAMETERS

Model	T_{eff} (1)	log g	log [Fe]	T_{spec}/T_{eff}
1	0.252	14	-5	1.76
2	0.501	14	-5	1.58
3	1.083	14	-5	1.47
4	1.079	14	-5	1.46
5	1.259	14	0	1.46
6	1.615	14	-5	1.56
7	0.253	15	-5	1.96
8	0.505	15	-5	1.69
9	1.008	15	-5	1.50
10	1.011	15	0	1.45
11	1.514	15	-5	1.43
12	1.507	15	0	1.38
13	2.023	15	-5	1.40
14	2.541	15	-5	1.45
15	2.850	15	-5	1.52
16(2)	2.860	15	-5	3.29
17(3)	2.842	14	--	1.39

Notes:

(1) T_{eff} is the effective temperature (in keV), g the gravity (in cm s^{-2}) and Fe the iron abundance (relative to solar, which is taken to be 3.4×10^{-5} by number relative to H). T_{spec} is the spectral temperature found by fitting a normalized Planck function to the calculated output specrtrum.

(2) Model 16 was constructed without Comptonization, that is assuming purely elastic electron scattering.

(3) Model 17 has an all He composition.

Table 2 **Surface Flux for Low and High Temperature Models**

T_{eff}	0.252	0.501	0.253	0.505		2.541	2.850	2.842
log g	14.000	14.000	15.000	15.000		15.000	15.000	15.000
log He	0.000	0.000	0.000	0.000		0.000	0.000	(all He)
log Fe	-5.000	-5.000	-5.000	-5.000		-5.000	-5.000	...
log hν					log hν			
-1.273	19.540	19.925	19.472	19.856	-0.672	22.295	22.379	22.324
-1.218	19.643	20.029	19.594	19.966	-0.618	22.391	22.475	22.420
-1.162	19.745	20.133	19.707	20.074	-0.564	22.485	22.570	22.515
-1.107	19.846	20.237	19.814	20.181	-0.510	22.578	22.663	22.609
-1.051	19.947	20.341	19.917	20.288	-0.456	22.671	22.754	22.704
-0.995	20.046	20.445	20.017	20.394	-0.402	22.764	22.844	22.798
-0.940	20.144	20.549	20.115	20.499	-0.348	22.855	22.934	22.892
-0.884	20.241	20.653	20.210	20.604	-0.294	22.945	23.022	22.985
-0.829	20.335	20.756	20.304	20.708	-0.240	23.034	23.108	23.077
-0.773	20.427	20.859	20.395	20.811	-0.186	23.121	23.192	23.168
-0.718	20.517	20.960	20.483	20.913	-0.132	23.205	23.273	23.257
-0.662	20.604	21.061	20.568	21.014	-0.078	23.288	23.351	23.345
-0.606	20.688	21.161	20.650	21.112	-0.024	23.369	23.426	23.433
-0.551	20.769	21.258	20.729	21.209	0.030	23.449	23.499	23.519
-0.495	20.846	21.354	20.804	21.303	0.084	23.526	23.569	23.603
-0.440	20.919	21.447	20.874	21.396	0.138	23.600	23.637	23.686
-0.384	20.987	21.538	20.941	21.485	0.192	23.671	23.703	23.765
-0.329	21.051	21.627	21.002	21.573	0.246	23.738	23.766	23.842
-0.273	21.109	21.712	21.058	21.657	0.300	23.802	23.827	23.915
-0.218	21.160	21.794	21.107	21.737	0.354	23.862	23.885	23.984
-0.162	21.204	21.872	21.149	21.814	0.408	23.920	23.943	24.050
-0.106	21.240	21.945	21.183	21.886	0.462	23.976	23.999	24.112
-0.051	21.266	22.012	21.209	21.953	0.516	24.030	24.056	24.171
0.005	21.281	22.072	21.226	22.015	0.570	24.084	24.112	24.228
0.060	21.284	22.125	21.233	22.071	0.624	24.136	24.170	24.281
0.116	21.273	22.169	21.230	22.119	0.678	24.186	24.228	24.331
0.171	21.247	22.202	21.213	22.159	0.731	24.235	24.285	24.379
0.227	21.202	22.224	21.182	22.189	0.785	24.280	24.340	24.424
0.283	21.138	22.234	21.135	22.208	0.839	24.321	24.392	24.465
0.338	21.051	22.230	21.070	22.215	0.893	24.355	24.439	24.501
0.394	20.940	22.212	20.983	22.207	0.947	24.380	24.478	24.529
0.449	20.801	22.178	20.874	22.183	1.001	24.393	24.508	24.548
0.505	20.633	22.128	20.738	22.141	1.055	24.391	24.526	24.555
0.560	20.430	22.057	20.573	22.079	1.109	24.371	24.529	24.546
0.616	20.189	21.964	20.376	21.995	1.163	24.330	24.515	24.518
0.671	19.900	21.841	20.142	21.887	1.217	24.263	24.479	24.466
0.727	19.554	21.683	19.866	21.750	1.271	24.166	24.419	24.388
0.783	19.136	21.481	19.542	21.580	1.325	24.035	24.330	24.278
0.838	18.627	21.225	19.160	21.370	1.379	23.865	24.207	24.132
0.894	17.996	20.908	18.705	21.112	1.433	23.649	24.047	23.944
0.949	17.194	20.518	18.153	20.795	1.487	23.381	23.844	23.708
1.005	16.139	20.044	17.460	20.407	1.541	23.056	23.591	23.418
1.060	14.841	19.470	16.587	19.936	1.595	22.664	23.283	23.067
1.116	13.227	18.768	15.490	19.366	1.649	22.200	22.911	22.649
1.172	11.277	17.909	14.107	18.669	1.703	21.656	22.467	22.160
1.227	9.099	16.847	12.395	17.789	1.757	21.023	21.944	21.585
1.283	6.980	15.523	10.394	16.705	1.811	19.980	21.335	20.747
1.338	4.853	13.858	8.483	15.353	1.865	18.477	20.545	19.643
1.394	2.557	11.645	6.438	13.631	1.919	16.474	18.732	18.145
1.449	0.141	8.897	4.192	11.160	1.973	13.797	16.260	16.068

Table 3 **Surface Flux for Mid Temperature Models**

T_{eff}	1.083	1.079	1.259	1.615	1.008	1.011	1.514	1.507	2.023
log g	14.000	14.000	14.000	14.000	15.000	15.000	15.000	15.000	15.000
log He	0.000	0.000	0.000	0.000	0.000	0.000	0.000	0.000	0.000
log Fe	−5.000	0.000	−5.000	−5.000	−5.000	0.000	−5.000	0.000	−5.000
log hν									
−0.972	21.125	21.096	21.286	21.538	20.892	20.871	21.267	21.268	21.567
−0.917	21.221	21.189	21.380	21.637	20.995	20.978	21.364	21.365	21.666
−0.861	21.317	21.283	21.475	21.734	21.099	21.085	21.462	21.462	21.763
−0.806	21.413	21.377	21.571	21.829	21.202	21.191	21.561	21.558	21.860
−0.750	21.509	21.471	21.667	21.923	21.305	21.298	21.659	21.654	21.955
−0.694	21.605	21.566	21.763	22.015	21.408	21.403	21.757	21.749	22.051
−0.639	21.702	21.662	21.858	22.106	21.512	21.508	21.856	21.845	22.147
−0.583	21.799	21.759	21.954	22.197	21.616	21.613	21.954	21.940	22.243
−0.528	21.896	21.856	22.049	22.287	21.719	21.716	22.052	22.036	22.339
−0.472	21.993	21.953	22.144	22.374	21.822	21.818	22.150	22.132	22.435
−0.417	22.090	22.050	22.238	22.460	21.923	21.920	22.248	22.229	22.531
−0.361	22.185	22.147	22.332	22.543	22.024	22.020	22.346	22.325	22.626
−0.305	22.279	22.243	22.425	22.623	22.124	22.120	22.444	22.422	22.720
−0.250	22.372	22.338	22.515	22.700	22.221	22.217	22.540	22.519	22.815
−0.194	22.463	22.431	22.604	22.775	22.315	22.313	22.636	22.615	22.909
−0.139	22.551	22.521	22.690	22.849	22.407	22.407	22.731	22.710	23.002
−0.083	22.636	22.608	22.772	22.920	22.496	22.499	22.825	22.805	23.094
−0.028	22.718	22.692	22.851	22.989	22.583	22.588	22.918	22.899	23.184
0.028	22.795	22.771	22.926	23.054	22.667	22.674	23.008	22.990	23.271
0.083	22.867	22.845	22.997	23.116	22.747	22.756	23.095	23.078	23.356
0.139	22.933	22.914	23.063	23.176	22.823	22.833	23.179	23.163	23.437
0.195	22.994	22.976	23.125	23.234	22.894	22.905	23.258	23.244	23.515
0.250	23.049	23.033	23.181	23.290	22.959	22.971	23.332	23.321	23.588
0.306	23.099	23.084	23.233	23.345	23.016	23.030	23.402	23.392	23.658
0.361	23.142	23.130	23.281	23.401	23.066	23.081	23.465	23.457	23.723
0.417	23.180	23.170	23.325	23.458	23.106	23.123	23.522	23.516	23.783
0.472	23.213	23.204	23.365	23.513	23.137	23.155	23.572	23.568	23.839
0.528	23.240	23.233	23.401	23.568	23.157	23.177	23.615	23.613	23.890
0.584	23.259	23.254	23.431	23.620	23.165	23.188	23.652	23.651	23.938
0.639	23.268	23.266	23.454	23.669	23.162	23.187	23.682	23.683	23.982
0.695	23.264	23.265	23.467	23.711	23.144	23.173	23.704	23.707	24.021
0.750	23.243	23.248	23.466	23.744	23.111	23.144	23.716	23.724	24.055
0.806	23.200	23.210	23.448	23.766	23.058	23.097	23.717	23.730	24.082
0.861	23.129	23.149	23.407	23.774	22.979	23.028	23.703	23.724	24.100
0.917	23.027	23.060	23.340	23.764	22.871	22.931	23.668	23.703	24.105
0.972	22.886	22.921	23.241	23.733	22.724	22.723	23.610	23.649	24.094
1.028	22.700	22.633	23.104	23.677	22.533	22.343	23.521	23.499	24.062
1.084	22.463	22.329	22.923	23.590	22.289	21.980	23.397	23.328	24.006
1.139	22.171	22.001	22.692	23.470	21.984	21.625	23.231	23.138	23.920
1.195	21.806	21.634	22.403	23.309	21.611	21.252	23.017	22.917	23.799
1.250	21.366	21.201	22.050	23.103	21.156	20.836	22.750	22.655	23.637
1.306	20.831	20.687	21.631	22.844	20.608	20.344	22.419	22.334	23.428
1.361	20.193	20.068	21.110	22.524	19.949	19.754	22.015	21.943	23.166
1.417	19.416	19.302	20.485	22.137	19.129	19.023	21.531	21.473	22.843
1.473	18.441	18.360	19.716	21.672	18.118	18.087	20.948	20.902	22.452
1.528	17.238	17.173	18.780	21.119	16.784	16.896	20.248	20.220	21.993
1.584	15.560	15.533	17.547	20.470	15.077	15.269	19.371	19.359	21.429
1.639	13.490	13.492	15.934	19.701	12.646	13.027	18.280	18.287	20.729
1.695	10.642	10.832	13.804	18.278	9.444	10.931	16.785	16.807	19.851
1.750	6.942	8.529	10.840	16.187	7.137	8.976	14.652	14.684	18.666

Postal Addresses:

W. Michael Howard and Richard A. London, University of California, Lawrence Livermore National Laboratory, Livermore, California 94550

Ronald E. Taam, Department of Physics and Astronomy, Northwestern University, Evanston, IL 60201

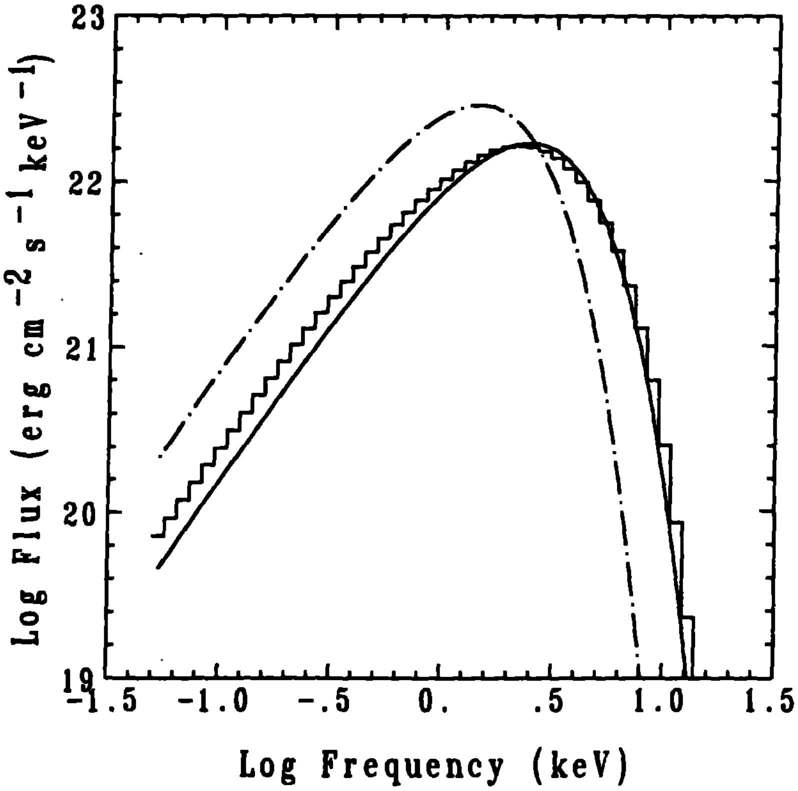

23
22
21
20
19
-1.5
-1.0
-.5
0.
.5
1.0
1.5
Log Flux (erg cm^{-2} s^{-1} keV^{-1})
Log Frequency (keV)

Fig. 1

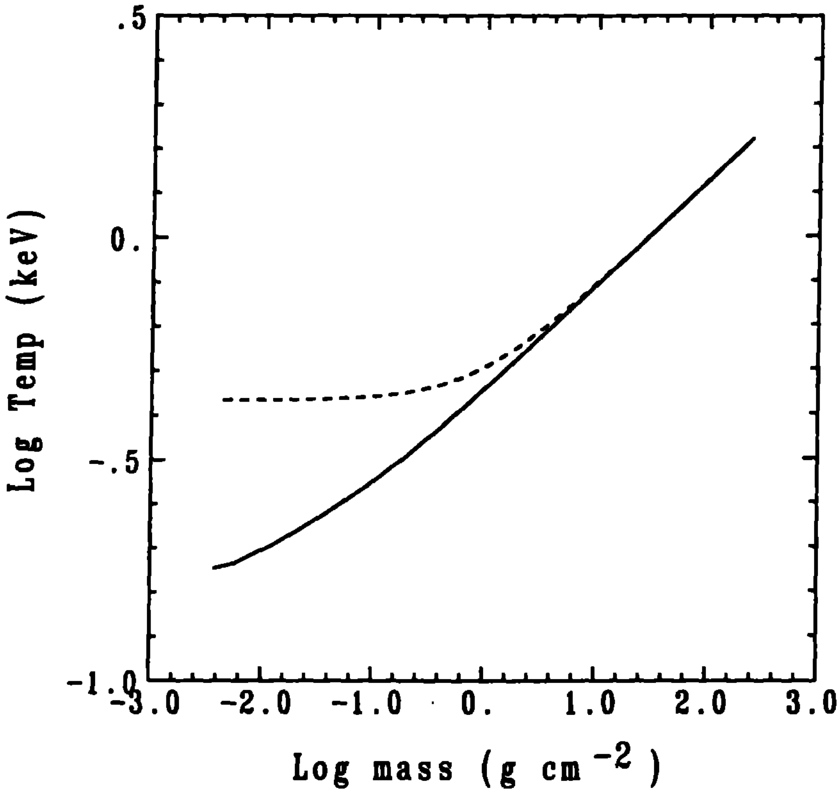

Fig. 2

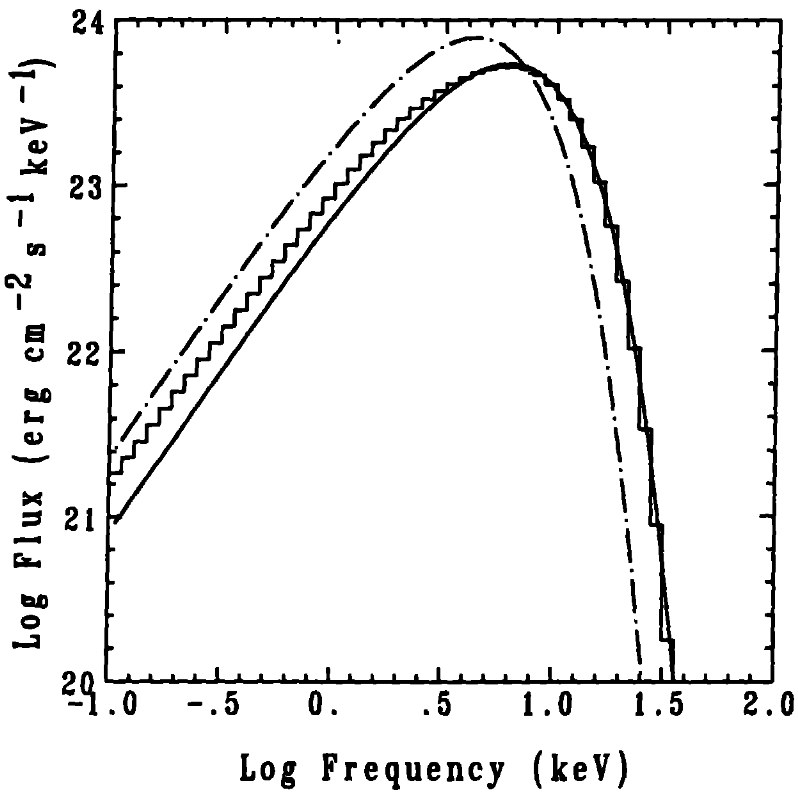

Log Flux (erg cm^{-2} s^{-1} keV^{-1})
24
23
22
21
20
-1.0
-.5
0.
.5
1.0
1.5
2.0
Log Frequency (keV)

Fig. 3

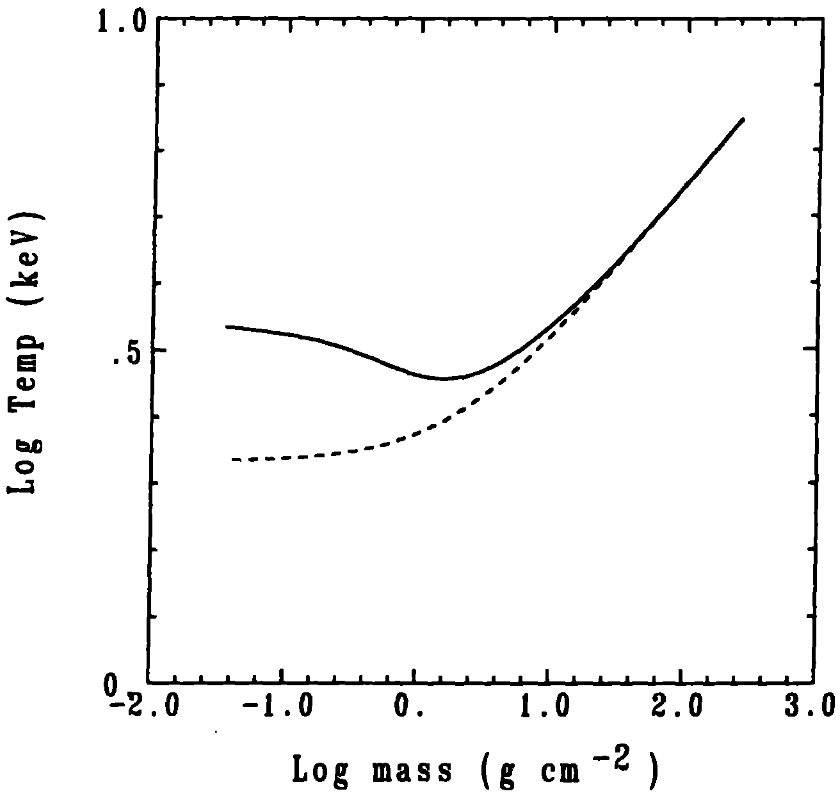

Fig. 4

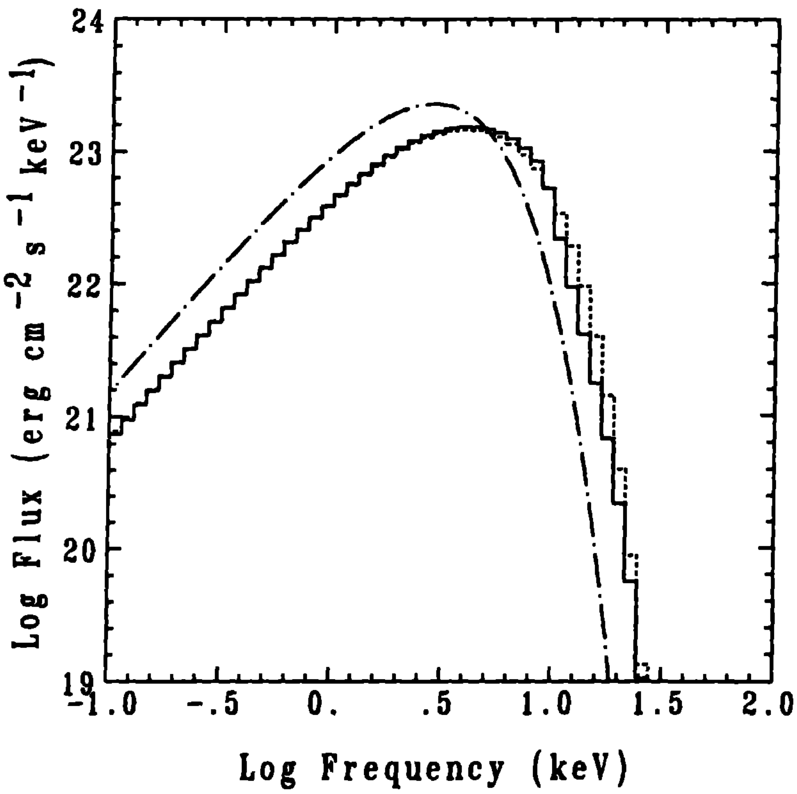
24
23
22
21
20
19
-1.0
-.5
0.
.5
1.0
1.5
2.0
Log Flux (erg cm^{-2} s^{-1} keV^{-1})
Log Frequency (keV)

Fig. 5

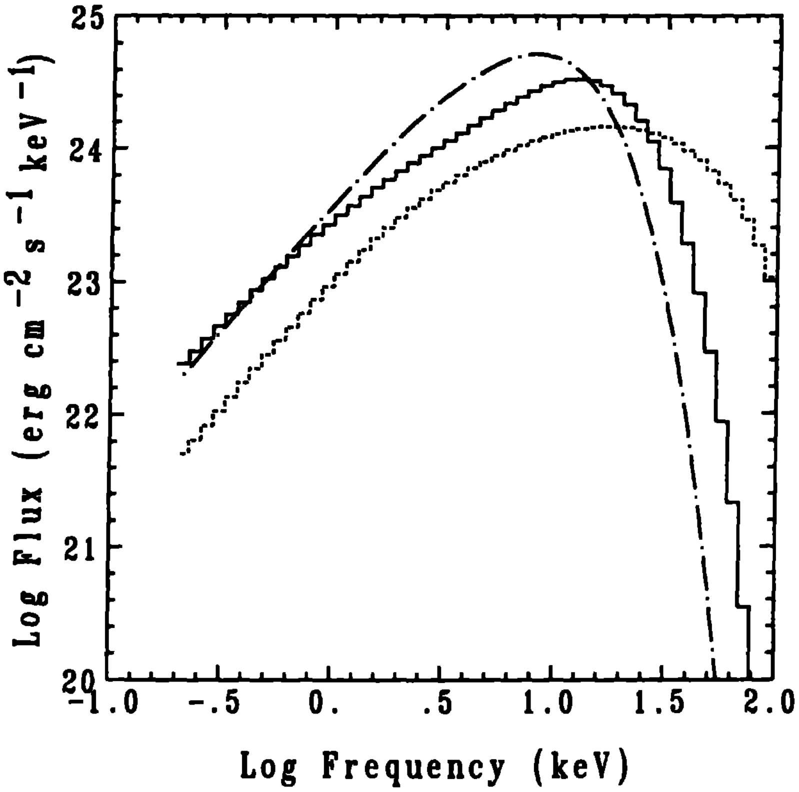
25
24
23
22
21
20
-1.0
-.5
0.
.5
1.0
1.5
2.0
Log Flux (erg cm^{-2} s^{-1} keV^{-1})
Log Frequency (keV)

Fig. 6

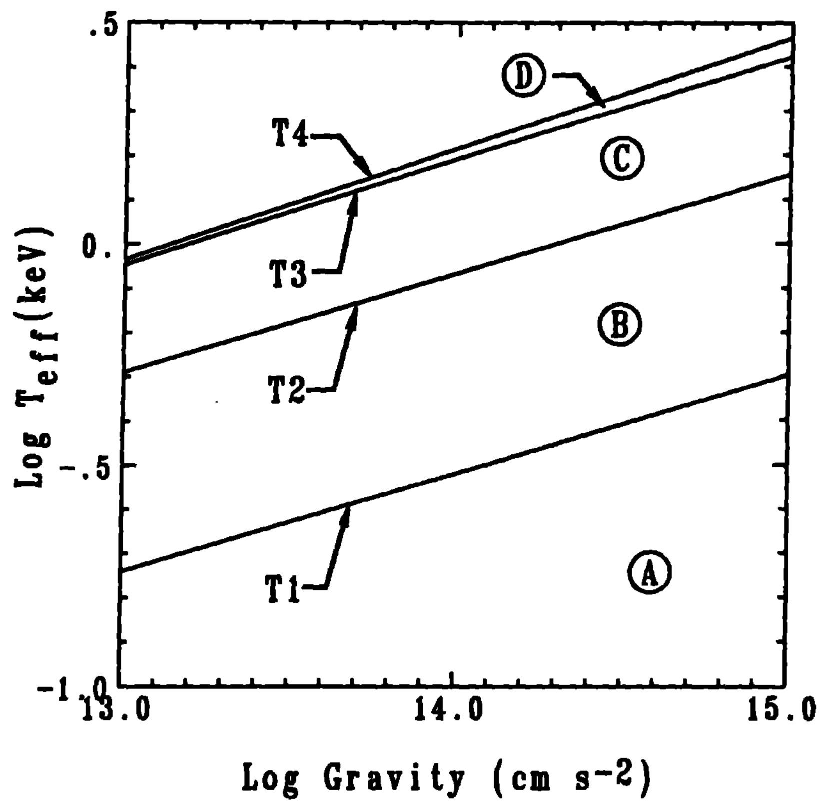
.5
0.
-.5
-1.0
13.0
14.0
15.0
Log Gravity (cm s-2)
Log Teff(keV)
D
C
B
A
T4
T3
T2
T1

Fig. 7